Periodic orbit bifurcations and local symmetry restorations in exotic-shape nuclear mean fields

Periodic orbit bifurcations and local symmetry restorations in exotic-shape nuclear mean fields

Ken-ichiro Arita

Department of Physics, Nagoya Institute of Technology, Nagoya 466-8555, Japan

E-mail: arita@nitech.ac.jp

Submitted: 28 February 2017
Published: 20 June 2017 in Phys. Scr. **92**, 074005

Abstract
The semiclassical origins of the enhancement of shell effects in exotic-shape mean-field potentials are investigated by focusing attention on the roles of the local symmetries associated with the periodic-orbit bifurcations. The deformed shell structures for four types of pure octupole shapes in the nuclear mean-field model having a realistic radial dependence are analyzed. Remarkable shell effects are shown for a large Y_{32} deformation having tetrahedral symmetry. Much stronger shell effects found in the shape parametrization smoothly connecting the sphere and the tetrahedron are investigated from the view point of the classical-quantum correspondence. The local dynamical symmetries associated with the bridge orbit bifurcations are shown to have significant roles in emergence of the exotic deformed shell structures for certain combinations of the surface diffuseness and the tetrahedral deformation parameters.

Keywords: periodic orbit theory, nuclear tetrahedral deformation, shell structure

1. Introduction

The relative stabilities of atomic nuclei are essentially determined by single-particle shell effects [1–3]. The properties of nuclear shell structures are strongly dependent on the symmetries of the mean-field potential. In the nuclear potentials with a spherical symmetry, shell structures are greatly developed and one has distinct magic numbers corresponding to shell closures ($N, Z = 2, 8, 20, 28, 50, 82, 126, \cdots$). As the origin of such remarkable shell structures, both the spherical symmetry and the effect of an approximate dynamical symmetry called pseudo SU(3) are important [4]; the latter causes bunchings of levels with different angular momenta.

The roles of dynamical symmetries are more important in establishing deformed shell structures. The origins of super- and hyperdeformations, denoting extraordinarily large quadrupole deformations whose axis ratios are 2:1 and 3:1, can be simply accounted for as the results of the dynamical symmetries of the harmonic oscillator models with rational frequency ratios [5]. In more realistic mean-field potentials having sharper surfaces, approximate (weakly broken) dynamical symmetries should play roles. In general, the existence of such dynamical symmetries is hidden and not found by just looking at the Hamiltonian.

We would like to point out the fact that the dynamical symmetries are reflected in the stability properties of the classical periodic orbits (POs). Therefore, the semiclassical periodic-orbit theory (POT) [6–9] is a good tool to investigate the relationship between the quantum shell effect and the dynamical symmetries. We will pay special attention to the bifurcations of the classical POs, which are related to the local dynamical symmetries restored in the phase space around the orbits [10].

Although the quadrupole deformations play the most important role in lowering the energies of nuclei away from the spherical shell closures, other types of shape degrees of freedom, such as octupoles, also become significant in certain particle-number regions [11]. Since the shell effects associated with octupole deformations are generally weaker than those for quadrupole ones, protons and neutrons should play constructive roles to realize such deformations. Recent development of experiments opens the door to exploration of various combinations of N and Z considerably far from the stability line, and the possibilities of tetrahedral-shape nuclei attract greater attention from both the theoretical and experimental sides [12–15]. In several theoretical mean-field calculations, it is indicated that the Y_{32} shape degree of freedom having tetrahedral symmetry is very important and the potentials with the tetrahedral-type deformations show strong shell effects [12, 16, 17]. In addition to the geometrical degeneracies due to the point-group symmetry, strong bunching of levels belonging to different irreps are found. Hamamoto *et al* tried to understand the reason for this gross shell effect by looking at how the degeneracy of

$\Delta l = 3$ levels in the spherical limit resolves by the octupole perturbations [16], but its relation to dynamical symmetries has not been considered. It is very interesting to notice that, in a Woods-Saxon (WS) type potential without spin-orbit coupling, the tetrahedral magic numbers are identical to those of the spherical harmonic oscillator (HO) having the SU(3) dynamical symmetry [16, 17]. This may suggest that SU(3) dynamical symmetry is partially restored for certain combinations of the sharpness of the potential surface and the tetrahedral-type deformation.

In this paper, we first recapitulate the analysis of deformed shell structures for four types of pure octupole shapes using a nuclear mean-field potential model with a realistic radial dependence. We will show that anomalously strong shell effects are found for a shape parametrization interpolating the sphere and tetrahedron. Using the semiclassical POT, we will analyze the origin of the above tetrahedral shell structures and point out the important role by a special type of the PO bifurcation, called a bridge-orbit bifurcation [18]. The relationship between the dynamical symmetry restoration and PO bifurcations is discussed, and the semiclassical origins of exotic tetrahedral shell structures are clarified.

2. Shell structures in tetrahedral-shape potentials

In this section, the radial power-law (RPL) potential model is introduced to approximate the realistic WS type potential. With this simplified model, we examine the shell structures in octupole shapes and show that the Y_{32} type deformations having tetrahedral T_d symmetry give rise to strong shell effects.

2.1. The radial power-law (RPL) potential model

The nuclear mean-field potential is approximately described by the WS model

$$V_{\rm ws} = -\frac{V_0}{1+\exp\frac{r-R(A)}{a}} \tag{1}$$

with depth $V_0 \approx 50\,\mathrm{MeV}$, radius $R(A) \approx 1.3A^{1/3}\,\mathrm{fm}$ for the mass number A, and surface diffuseness $a \approx 0.7\,\mathrm{fm}$. This potential can be approximated by a HO potential for light nuclei, while it is rather closer to a square-well potential (which is further approximated by an infinite well) for heavier nuclei. In order to describe the nuclei in a wide range of mass numbers, we propose the RPL potential [18]

$$V(\boldsymbol{r}) = -V_0 + U_0 \cdot \left(\frac{r}{R_0}\right)^{\alpha}, \tag{2}$$

which nicely approximates the inner part ($r \lesssim R(A)$) of the WS potential (see figure 1). Eliminating the constant term in the potential (2), we define our model Hamiltonian as

$$H = \frac{p^2}{2M} + U_0 \cdot \left(\frac{r}{R_0 f(\theta,\varphi)}\right)^{\alpha} \tag{3}$$

with nucleon mass M, length unit R_0, energy unit $U_0 = \hbar^2/MR_0^2$, and a dimensionless function $f(\theta,\varphi)$ which describes the shape of the equi-potential surface. The sharpness of the potential surface is controlled by the power parameter α. The advantage of taking the RPL model in place of WS is the scaling property which makes our semiclassical analysis highly simple (see section 3 below). The Hamiltonian can be also extended to take account of the spin-orbit coupling keeping some advantages of the scaling property [10], but we neglect it in the current study for simplicity.

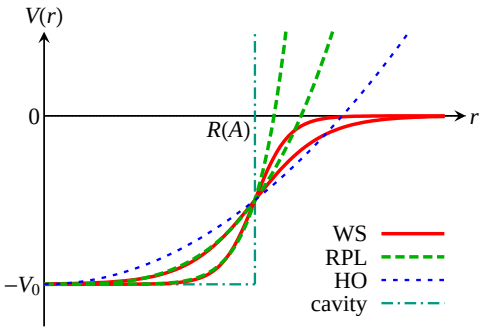

Figure 1. Comparison of the Woods-Saxon (WS), radial power-law (RPL), harmonic oscillator (HO, $\alpha = 2$) and cavity (infinite well, $\alpha = \infty$) potentials.

2.2. Evolution of the shell structure with pure octupole deformations

Hamamoto *et al* have examined the deformed shell structures for the four types of pure octupole shapes by adding the octupole field to the modified oscillator potential without spin-orbit coupling as

$$V = \frac{1}{2}m\omega_0^2 r^2\left\{1+\varepsilon_{3\mu}\frac{Y_{3\mu}+Y_{3\mu}^*}{\sqrt{2(1+\delta_{\mu 0})}}\right\} + V_{ll}, \tag{4}$$

and have obtained remarkable shell gaps for Y_{32} deformation around $\varepsilon_{32} \approx 0.5$ [16]. In the central part of the potential (4), the shape of the equi-potential surface reads

$$R(\theta,\varphi;\varepsilon_{32}) = R_0\left[1+\varepsilon_{32}\frac{Y_{32}+Y_{32}^*}{\sqrt{2}}\right]^{-1/2}. \tag{5}$$

Dudek *et al* investigated the tetrahedral shell structures using the realistic WS potential with spin-orbit coupling [12,13]. The shape of the potential surface is parametrized as

$$R(\theta,\varphi;t_3) = R_0\Big\{1+t_3(Y_{32}+Y_{3-2}^*)+\cdots\Big\}. \tag{6}$$

They also obtained remarkable shell gaps at a large Y_{32} deformation $t_3 \approx 0.3$ in the single-particle level diagram. Thus, one sees that the tetrahedral-type shape degrees of freedom play significant roles in the nuclear dynamics.

The shape parametrizations (5) and (6) are equivalent for small Y_{32} deformations but become considerably different for large deformations. These parametrizations can be generalized into the form

$$R(\theta,\varphi) = R_0\left[1+k\beta_{3\mu}\frac{Y_{3\mu}+Y_{3\mu}^*}{\sqrt{2(1+\delta_{\mu 0})}}\right]^{1/k}, \tag{7}$$

where (5) and (6) corresponds to the case $k=-2$ and $k=1$, respectively, with $\beta_{32} = 2\varepsilon_{32} = \sqrt{2}t_3$. We determine the parameter k to minimize the surface area under volume conservation

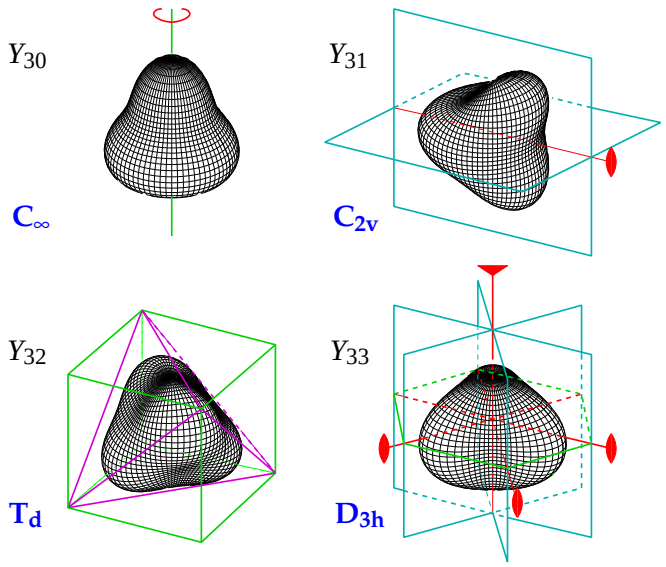

Figure 2. Shapes and symmetries of the potential surfaces for the pure octupole deformations (8) with $\beta_{3\mu} = 0.3$.

condition, and obtained the value $k \approx 0$ for all four types of octupole deformations. Using the relation $\lim_{k\to 0}(1+kx)^{1/k} = e^x$, we define the shape function f in equation (3) as

$$f(\Omega;\beta_{3\mu}) = \exp\left[\beta_{3\mu}\frac{Y_{3\mu}+Y_{3\mu}^*}{\sqrt{2(1+\delta_{\mu 0})}}\right]. \tag{8}$$

The shapes of the equi-potential surfaces are displayed in figure 2. Each shape has its own continuous or discrete point-group symmetry and the quantum levels are classified by the irreducible representations (irreps) of the group. The Y_{30} shape is axially symmetric (C_∞) and the single-particle levels are classified by the magnetic quantum number K. All the levels except $K = 0$ are doubly degenerate due to the time-reversal symmetry. The Y_{31} and Y_{33} shapes have discrete symmetries C_{2v} and D_{3h}, respectively. The group C_{2v} has only 1-dimensional irreps while D_{3h} has 2-dimensional irreps in addition which provide doubly degenerate levels. The Y_{32} shape has the tetrahedral symmetry T_d, which consists of 24 symmetry transformations and has 3-dimensional irreps. The levels belonging to the 3-dimensional irreps are triply degenerate and, thus, one can expect larger shell effects compared with the other three. For each deformation, single-particle level diagrams are shown in figure 3. With increasing $\beta_{3\mu}$, one finds a remarkable enhancement of the shell effect at a large Y_{32} deformation around $\beta_{32} = 0.3 \sim 0.4$, where large and regular equi-distant shell gaps appear. The particle numbers corresponding to the shell closures are $2, 8, 20, 40, 70, 112, 168, 240, \cdots$, which are identical to those for the spherical HO model. This coincidence is hard to believe as just incidental, and we expect a kind of a symmetry restoration taking place for this octupole potential.

2.3. Anomalous shell effect at large tetrahedral deformation

In the pure Y_{32} deformation, potential surface suffers concavity at large β_{32} and the classical dynamics becomes strongly chaotic. In general, the quantum shell effect is moderate in a classically chaotic system. Thus, it might be favorable to evolve a tetrahedral-type deformation keeping convexity of the

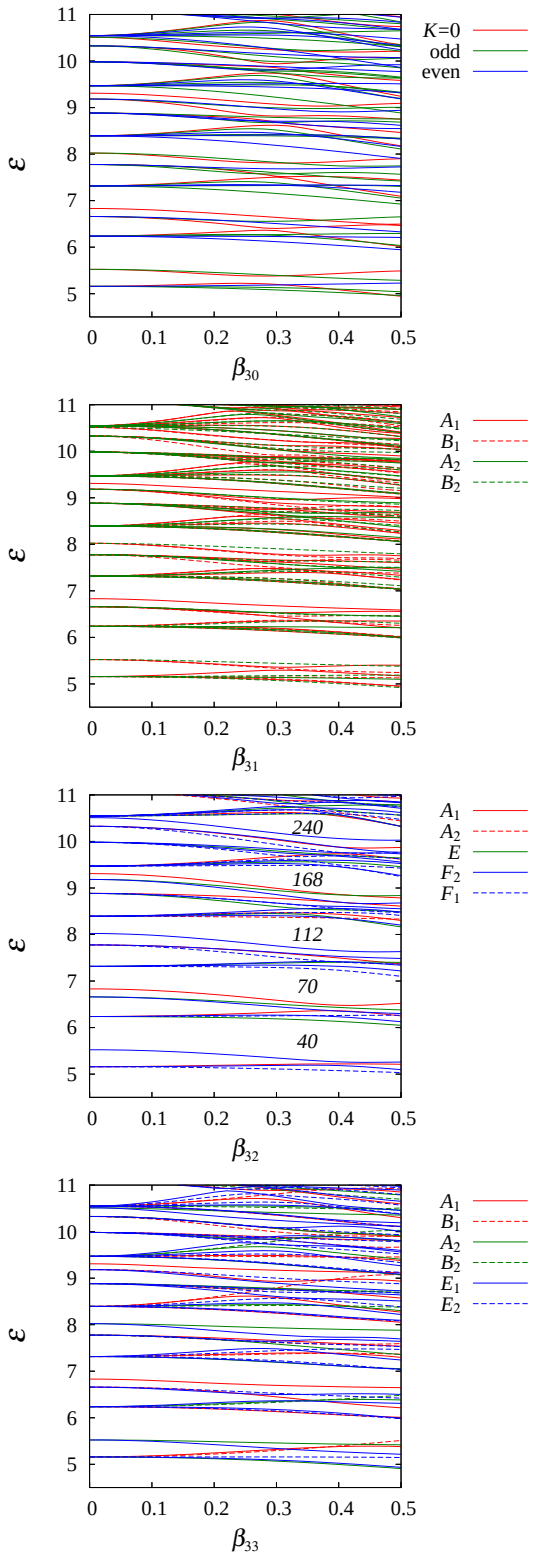

Figure 3. Single-particle level diagrams of the RPL potential model with the power parameter $\alpha = 5.0$ for four types of pure octupole deformations. Values of the scaled energy $\mathcal{E}$ (see equation (19)) for the single-particle eigenstates, $\mathcal{E}_i = (e_i/U_0)^{1/\alpha+1/2}$, are plotted as functions of the octupole parameter $\beta_{3\mu}$. For $\mu = 0$, levels are classified by the magnetic quantum number K. For $\mu \neq 0$, levels are classified by the irreps of the point group symmetries. 1-dimensional (A_i, B_i), 2-dimensional (E_i) and 3-dimensional (F_i) irreps are singly, doubly and triply degenerated, respectively. In the 3rd panel from the top, the particle number of the shell closures at large β_{32} are indicated with italics.

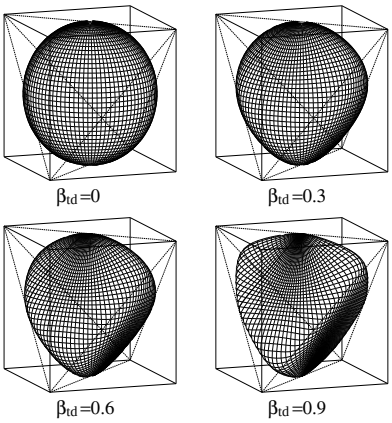

Figure 4. Shapes of the equi-potential surfaces with the shape function (9) for several values of the tetrahedral parameter $\beta_{\rm td}$.

surface in obtaining a stronger tetrahedral shell effect. We consider a shape parametrization which smoothly interpolates the sphere and tetrahedron with a single parameter $\beta_{\rm td}$ [19]. The shape function f is obtained by the least positive root of the following quartic equation at each pair of angles (θ, φ),

$$f^2 + \beta_{\rm td}\left\{\frac{1}{2} + \left(\frac{2}{15}P_{32}(\zeta)\sin 3\varphi\right)f^3 - \left(\frac{1}{10} + \frac{2}{5}P_{40}(\zeta) + \frac{1}{420}P_{44}(\zeta)\cos 4\varphi\right)f^4\right\} = 1, \qquad (9)$$

with $\zeta = \cos\theta$. $\beta_{\rm td} = 0$ and 1 correspond to the sphere and tetrahedron, respectively, and one can continuously change the shape from a sphere to a tetrahedron by varying $\beta_{\rm td}$ from 0 to 1, keeping the convexity everywhere on the surface. The shapes of the equi-potential surfaces at several values of $\beta_{\rm td}$ are displayed in figure 4. Single-particle levels of the RPL Hamiltonian with the tetrahedral deformation are shown in figure 5. The tetrahedral shell effect in this shape parametrization is found to be more pronounced than that of the pure Y_{32} shape as we expected. For sufficiently large values of the power parameter α, we always have the strong bunchings of levels at a large $\beta_{\rm td}$, whose value becomes larger as α increases, and have the same deformed magic numbers exactly identical to those of the spherical HO. In figure 6, evolutions of the shell energies $\delta E_{\rm sh}(N)$ are shown for several values of the tetrahedral parameter $\beta_{\rm td}$. A regular and strong shell effect is found at a large tetrahedral deformation $\beta_{\rm td} \sim 0.8$, which is quite similar to that for the spherical HO.

The above results suggest an emergence of a dynamical symmetry like SU(3) restored by a certain combination of the sharp potential surface and the tetrahedral deformation. As we mentioned in the introduction, dynamical symmetries are not easy to identify, as they are called hidden symmetries, especially when they are approximate ones, but one can find their signs in the properties of classical POs. In what follows, we will investigate the semiclassical origin of the above outstanding shell effect at exotic tetrahedral shapes using the POT.

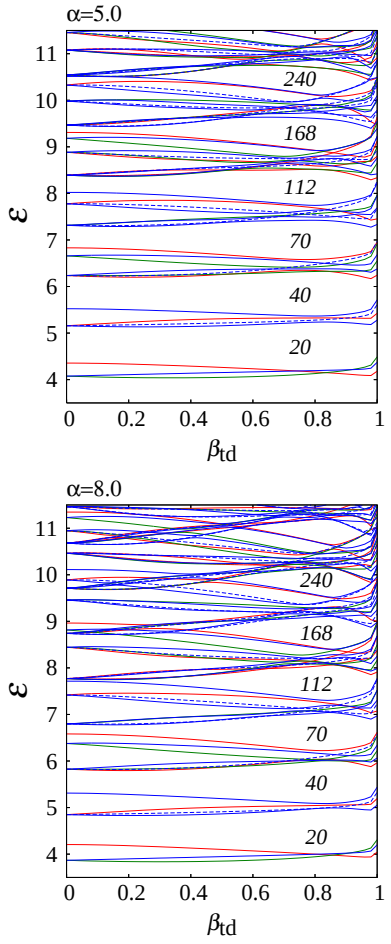

Figure 5. Single-particle level diagrams of the RPL potential models with radial power parameter $\alpha = 5.0$ (top panel) and 8.0 (bottom panel) for tetrahedral deformation. Scaled energy levels are plotted as the functions of tetrahedral parameter $\beta_{\rm td}$. The levels are classified by the irreps of the T_d group as for the Y_{32} deformation in figure 3. The particle numbers corresponding to the shell closures at large $\beta_{\rm td}$ are indicated with italics.

3. Semiclassical analysis of the tetrahedral shell structure

3.1. Trace formula

In the semiclassical trace formula [6–9], the single-particle level density is given by the sum over contributions of the classical POs

$$g(e) = \bar{g}(e) + \sum_{\rm PO} A_{\rm PO}(e)\cos\left(\frac{1}{\hbar}S_{\rm PO}(e) - \frac{\pi}{2}\mu_{\rm PO}\right). \qquad (10)$$

Here, $\bar{g}(e)$ is the average level density which is generally a monotonous function of energy. In the second term, representing the oscillating part, the sum is taken over all the classical POs including the repetitions of the primitive ones. The amplitude factor $A_{\rm PO}$ is determined by the period, degeneracy and stability of the orbit, $S_{\rm PO} = \oint_{\rm PO} \boldsymbol{p}\cdot d\boldsymbol{r}$ is the action integral, and $\mu_{\rm PO}$ is related to the Maslov index determined by geometric property of the orbit.

The derivation of the trace formula is based on the path inte-

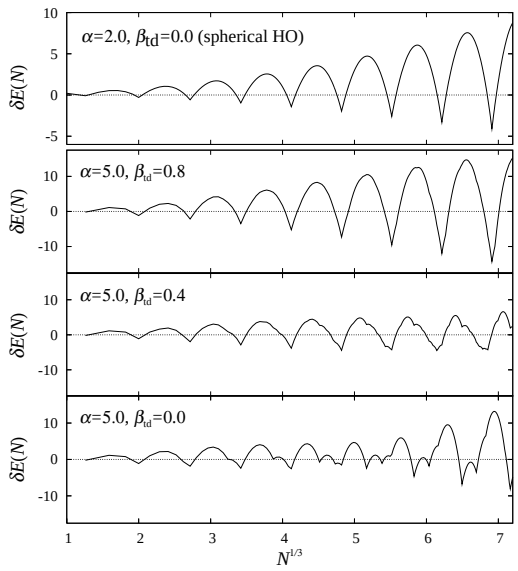

Figure 6. Shell energies $\delta E(N)$ for several values of the tetrahedral parameters $\beta_{\rm td}$ in the RPL potential model with $\alpha = 5.0$ (lower 3 panels), and those for the spherical HO (top panel, in a different energy unit).

gral representation of the transition amplitude

$$K(\boldsymbol{r}'', t''; \boldsymbol{r}', t') = \langle \boldsymbol{r}''| e^{-i\hat{H}(t''-t')/\hbar} |\boldsymbol{r}'\rangle = \int \mathcal{D}\boldsymbol{r} \exp\left[\frac{i}{\hbar}\int_{t'}^{t''} L(\boldsymbol{r}, \dot{\boldsymbol{r}})dt\right], \tag{11}$$

where $\hat{H}$ is the Hamiltonian operator, $\mathcal{D}\boldsymbol{r}$ is the integration measure for the path $\boldsymbol{r}(t)$ with $\boldsymbol{r}(t') = \boldsymbol{r}'$ and $\boldsymbol{r}(t'') = \boldsymbol{r}''$, and L represents the Lagrangian function. In the semiclassical limit where action quantities are sufficiently larger than the Plank's constant $\hbar$, the path integral in (11) can be evaluated by the stationary-phase approximation (SPA): for smooth functions $A(q)$ and $R(q)$ of a variable q, one has

$$\int A(q) e^{iR(q)/\hbar} dq \simeq \sum_i \sqrt{\frac{2\pi i\hbar}{R''(q_i^*)}} A(q_i^*) e^{iR(q_i^*)/\hbar}, \tag{12}$$

where q_i^* denotes the stationary point of the phase function $R(q)$ satisfying $R'(q_i^*) = 0$. The stationary condition for the path integral (11) is nothing but the Hamilton principle of the stationary action, and thus, the contributions associated with the classical trajectories connecting $\boldsymbol{r}'$ and $\boldsymbol{r}''$ are extracted. Then, it is inserted into the level density

$$g(e) = \int \langle \boldsymbol{r}|\delta(E - \hat{H})|\boldsymbol{r}\rangle d\boldsymbol{r} = \frac{1}{2\pi\hbar}\int d\boldsymbol{r} \int_{-\infty}^{\infty} dt e^{iet/\hbar} K(\boldsymbol{r}, t; \boldsymbol{r}, 0). \tag{13}$$

Carrying out the integrations over t and $\boldsymbol{r}(= \boldsymbol{r}' = \boldsymbol{r}'')$ in Eq. (13) by the SPA, one obtains the contribution of the POs at energy e. It is important to note that each term in the PO sum includes the contribution of neighboring trajectories, which is reflected in the amplitude factor $A_{\rm PO}$ as its dependency on the stability of the PO.

The energy dependence of the phase factor in Eq. (10) is given by the action integral $S_{\rm PO}(e)$, which is a monotonically increasing function of energy e, and thus, the contribution of each PO gives a regularly oscillating function of energy. The period of the oscillations with respect to energy,

$$\delta e = \frac{2\pi\hbar}{dS_{\rm PO}(e)/de} = \frac{2\pi\hbar}{T_{\rm PO}}, \tag{14}$$

is inversely proportional to the time period $T_{\rm PO}$ of the orbit, and therefore, the gross structure of the level density (corresponding to large δe) is associated with the short POs.

The outline of the semiclassical analyses of the shell structure is illustrated in figure 7. On the left-hand side of the figure, the top panel shows a typical example of the oscillating part of the level density averaged over a certain resolution, which generally shows a complicated pattern. According to the semiclassical trace formula (10), such an oscillation can be always decomposed into several regular oscillations (as in the left lower panels): the slow oscillations as shown in $\delta g_{\rm S}$ are given by the short orbits (having small periods τ) which contribute to the gross shell structures, while the rapid oscillations as shown in $\delta g_{\rm L}$ are given by the longer orbit (having large τ) which contribute to the finer shell structures. As will be described below, the Fourier transform of the level density (the right-hand panel) exhibits peaks at the periods of those POs, and the heights of the peaks represent the magnitude of the orbits' contributions to the level density.

Using the formula (10), one can derive the trace formula for the shell energy [9, 20, 21]

$$\delta E(N) = \sum_{\rm PO}\left(\frac{\hbar}{T_{\rm PO}(e_F)}\right)^2 A_{\rm PO}(e_F) \times \cos\left(\frac{1}{\hbar}S_{\rm PO}(e_F) - \frac{\pi}{2}\mu_{\rm PO}\right), \tag{15}$$

where e_F is the Fermi energy determined as the function of the particle number N to satisfy

$$2\int_0^{e_F} g(e)de = N, \tag{16}$$

taking account of the spin degeneracy factor 2. One should note that, due to the extra factor proportional to $(T_{\rm PO})^{-2}$ in (15), contribution of long orbits are suppressed, and only some shortest POs contribute to the shell energy.

It is known that the shell structure is generally sensitive to the shape of the mean-field potential. This can be understood from the sensitivity of the stabilities of classical POs to the potential shape. In particular, as will be discussed in the following subsections, bifurcations of the POs have strong effects on the oscillating part of the level density at which the orbits change from stable to unstable. Thus, we focus on the bifurcations of the short POs, which play important roles in evolutions of the deformed shell structures.

3.2. Classical periodic orbits in the RPL potential

In order to clarify the semiclassical origin of the tetrahedral shell structures, we first consider the properties of the classical POs in the RPL potential.

Since the Hamiltonian (3) is homogeneous both in momenta and in coordinates, the following scaling relation holds:

$$c^{-1}H(c^{1/2}\boldsymbol{p}, c^{1/\alpha}\boldsymbol{r}) = H(\boldsymbol{p}, \boldsymbol{r}), \tag{17}$$

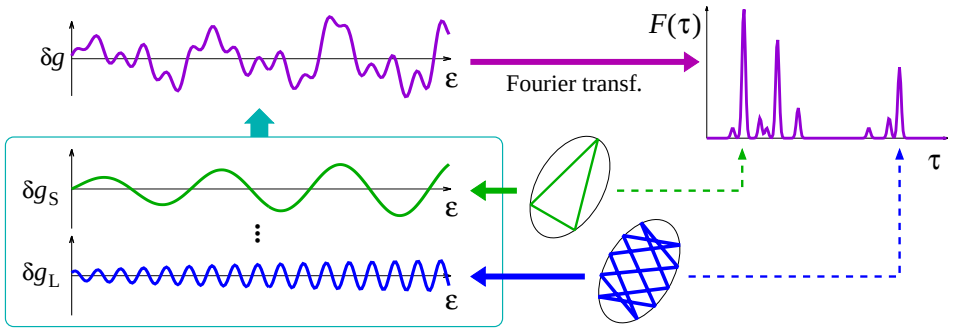

Figure 7. Illustration of the quantum-classical correspondence in the single-particle level density via the Fourier transformation. See the text for a detailed explanation.

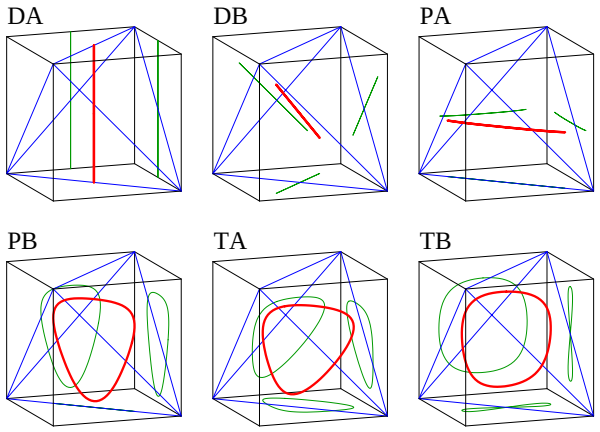

Figure 8. Some shortest POs in the tetrahedral RPL potential with $\alpha = 5.0$ and $\beta_{\rm td} = 0.3$. Their projections onto (x, y), (y, z) and (z, x) planes are also shown. The tetrahedron represents the symmetry of the potential.

and one can easily show the invariance of the equations of motion under the scaling transformation

$$\boldsymbol{p} \to c^{1/2}\boldsymbol{p}, \quad \boldsymbol{r} \to c^{1/\alpha}\boldsymbol{r}, \quad t \to c^{1/\alpha-1/2}t, \tag{18}$$

as energy $e \to ce$. Therefore, one will find the same set of classical POs independent of energy. This scaling property highly simplifies the semiclassical studies since the information on the POs at any energy e can be obtained by those calculated at a certain energy, e.g., $e = U_0$. When the tetrahedral deformation is added to the spherical RPL potential, the diameter and circle orbits bifurcate into three branches each. Two kinds of the straight-line orbits DA and DB along the three S_4 axes and the four C_3 axes, respectively, and curved self-retracing orbits PA in each of the mirror planes emerge from the diameter family. On the other hand, two kinds of three-dimensional rotational orbits TA, TB and planar ones PB emerge from the circle family. These six orbits are displayed in figure 8.

The contributions of these POs to the shell effect are manifested in the Fourier spectra of the quantum level density. Using the scaling relation, the action integral is found to be proportional to a simple power of energy:

$$S_{\rm PO}(e) = \left(\frac{e}{U_0}\right)^{\frac{1}{2}+\frac{1}{\alpha}} S_{\rm PO}(U_0) \equiv \mathcal{E}\hbar\tau_{\rm PO} \tag{19}$$

with the energy unit $U_0 = \hbar^2/MR_0^2$. In the last equation, we define the dimensionless "scaled energy" $\mathcal{E} \equiv (e/U_0)^{1/2+1/\alpha}$ and the energy-independent "scaled period" $\tau_{\rm PO} \equiv S_{\rm PO}(U_0)/\hbar$. The trace formula (10) is then rewritten in terms of these scaled variables $(\mathcal{E}, \tau)$ as

$$\begin{aligned} g(\mathcal{E}) &= g(e)\frac{de}{d\mathcal{E}} \\ &= g_0(\mathcal{E}) + \sum_{\rm PO} A_{\rm PO}(\mathcal{E})\cos(\tau_{\rm PO}\mathcal{E} - \tfrac{\pi}{2}\mu_{\rm PO}) \end{aligned} \tag{20}$$

Now we consider the Fourier transform of the scaled-energy level density

$$F(\tau) = \int d\mathcal{E}\, e^{i\tau\mathcal{E}} g(\mathcal{E}). \tag{21}$$

For the quantum level density $g(\mathcal{E}) = \sum_j \delta(\mathcal{E} - \mathcal{E}_j)$, one has

$$F^{\rm qm}(\tau) = \sum_j e^{i\tau\mathcal{E}_j}, \quad \mathcal{E}_j = (e_j/U_0)^{\frac{1}{2}+\frac{1}{\alpha}}, \tag{22}$$

which can be easily evaluated using the single-particle energy spectra $\{e_j\}$ calculated quantum-mechanically. Practically, we apply a triangular cut-off in which we multiply the integrand by the function $(1 - \mathcal{E}/\mathcal{E}_c)$ and evaluated the integral over $0 < \mathcal{E} < \mathcal{E}_c$. Inserting the semiclassical trace formula (20), one obtains the expression

$$F^{\rm cl}(\tau) = F_0(\tau) + \pi \sum_{\rm PO} e^{\frac{i\pi}{2}\mu_{\rm PO}} \widetilde{A}_{\rm PO}\delta(\tau - \tau_{\rm PO}). \tag{23}$$

$F(\tau)$ will thus have successive peaks at the scaled periods $\tau = \tau_{\rm PO}$ of the classical POs with the heights proportional to the amplitude $A_{\rm PO}$ of the corresponding orbits.

Figure 9 shows the moduli of the Fourier transforms $|F^{\rm qm}(\tau;\beta_{\rm td})|$ of the quantum level density for the RPL model with $\alpha = 5.0$ as functions of τ. At the spherical shape, $\beta_{\rm td} = 0$, one sees peaks at the diameter ($\tau = 5.06$) and circle ($\tau = 5.84$) orbits. With increasing tetrahedral deformation, the positions of these two peaks approach each other and merge into a single peak around $\tau = 5.6$, which shows the significant enhancement at $\beta_{\rm td} \simeq 0.6$. As we show below, this enhancement originates from the dynamical symmetry restoration associated with a special type of the PO bifurcation.

3.3. Bifurcation enhancement of the shell effect

As mentioned above, shell energies are essentially determined by the contributions of some shortest POs. The amplitude $A_{\rm PO}$

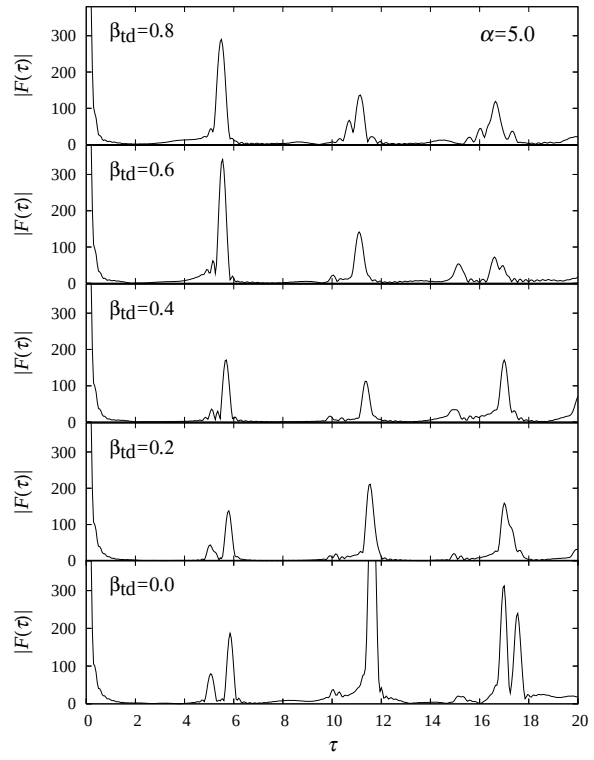

Figure 9. Fourier spectra of the single-particle level densities in the RPL potential ($\alpha = 5.0$). Moduli of the Fourier transform (22) are plotted as functions of τ for several values of the tetrahedral parameter $\beta_{\rm td}$.

depends on the shape mainly through the stability factor as

$$A_{\rm PO} \propto \frac{1}{\sqrt{|\det(I - M_{\rm PO})|}}, \tag{24}$$

where $M_{\rm PO}$ is the monodromy matrix which represents the linear stability of the orbit as described below. In the equi-energy surface $\{(\boldsymbol{p},\boldsymbol{r})|H(\boldsymbol{p},\boldsymbol{r}) = e\}$, consider a certain phase-space plane Σ perpendicular to the orbit. A classical trajectory starting off the point Z on Σ will subsequently cross Σ again at Z', and it defines a map $\mathcal{M}$ called the Poincaré map, $Z' = \mathcal{M}(Z)$. Periodic orbits $Z_{\rm PO}$ are the fixed points of the map $\mathcal{M}$, and the monodromy matrix is the linear part of $\mathcal{M}$ around the PO:

$$\mathcal{M}(Z_{\rm PO} + \delta Z) = Z_{\rm PO} + M_{\rm PO}\delta Z + O(\delta Z^2). \tag{25}$$

The factor $\det(I - M_{\rm PO})$ in (24) derives from the trace integral carried out by the SPA, and it is proportional to the curvature of the action $S(\boldsymbol{r};e)$ along the closed trajectory which starts from the point $\boldsymbol{r}$ with energy e and returns to $\boldsymbol{r}$ again,

$$S(\boldsymbol{r};e) = S(\boldsymbol{r}'',\boldsymbol{r}';e)|_{\boldsymbol{r}''=\boldsymbol{r}'=\boldsymbol{r}}, \quad S(\boldsymbol{r}'',\boldsymbol{r}';e) = \int_{\boldsymbol{r}'}^{\boldsymbol{r}''} \boldsymbol{p}\cdot d\boldsymbol{r}. \tag{26}$$

The stationary points of $S(\boldsymbol{r};e)$ correspond to the POs since the final momentum coincides with the initial momentum there:

$$\frac{\partial S(\boldsymbol{r};e)}{\partial \boldsymbol{r}} = \left(\frac{\partial S(\boldsymbol{r}'',\boldsymbol{r}';e)}{\partial \boldsymbol{r}''} + \frac{\partial S(\boldsymbol{r}'',\boldsymbol{r}';e)}{\partial \boldsymbol{r}'}\right)_{\boldsymbol{r}''=\boldsymbol{r}'=\boldsymbol{r}} = \boldsymbol{p}'' - \boldsymbol{p}' = 0. \tag{27}$$

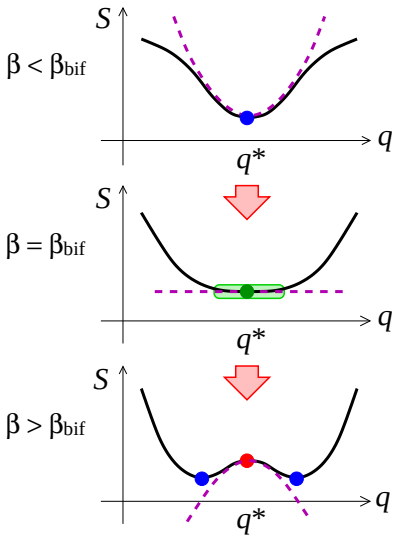

Figure 10. Illustration of the PO bifurcation and emergence of a local dynamical symmetry. Dots denote POs corresponding to the stationary point q^* of the action $S(q)$. Broken lines represent the quadratic approximation of $S(q)$ at the stationary points q^*. At the bifurcation point $\beta = \beta_{\rm bif}$, family of quasi-periodic orbits (shaded area) emerges around the periodic orbit q^*.

In general, the number of the stationary points changes when the curvature $\det(\partial^2 S/\partial\boldsymbol{r}\partial\boldsymbol{r})$ changes its sign. Therefore, the zeros of the curvature are accompanied by the PO bifurcations. Since the stability factor $\det(I - M_{\rm PO})$ is proportional to the curvature, the monodromy matrix $M_{\rm PO}$ has a unit eigenvalue at the bifurcation point (or a pair of unit eigenvalues depending on the bifurcation types), and the corresponding eigenvector δZ_1 gives the new bifurcated PO since it satisfies the periodic condition

$$\mathcal{M}(Z_{\rm PO} + \delta Z_1) \simeq Z_{\rm PO} + M_{\rm PO}\delta Z_1 = Z_{\rm PO} + \delta Z_1. \tag{28}$$

A typical bifurcation scenario known as a "pitchfork bifurcation" is illustrated in figure 10. In this case, the number of the POs changes from 1 to 3. Since the denominator in (24) approaches zero at the bifurcation point, one expects an enhancement of the amplitude there. The divergence of the amplitude at the bifurcation is due to the break-down of the standard SPA (12), and can be remedied by the use of the uniform approximation [22] which takes into account the higher-order expansions of the phase function, or by the improved SPA [23] which keeps the finite integration limits. This enhancement can be understood as the result of the local dynamical symmetry associated with the bifurcation. At the bifurcation point, the action function is approximately flat around the stationary point in the certain direction. This local invariance of the action against the change of coordinate indicates an appearance of a local dynamical symmetry. It generates a locally degenerate family of quasi-periodic orbits, which will make a coherent contribution to the trace integral. Actually, it often brings about a considerable enhancement of the amplitude factor $A_{\rm PO}$. This is the bifurcation enhancement of the quantum shell effect, which we consider as a significant semiclassical mechanism for exotic-shape states to be realized in finite fermion systems.

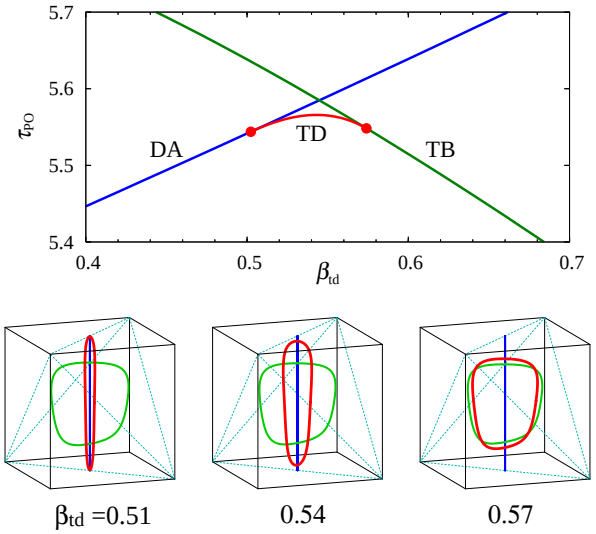

Figure 11. Classical POs participating one of the bridge bifurcations. The bridge orbit TD (red line) emerges from the diameter orbit DA (blue line) at $\beta_{td} = 0.502$ and submerges into the three-dimensional rotational orbit TB (green line) at $\beta_{td} = 0.574$. In the top panel, scaled period τ_{PO} of these orbits are plotted as functions of β_{td}. In the lower panel, shapes of those orbits at three values of β_{td} between the left and right ends of the bridge are displayed.

3.4. Bridge orbit bifurcation and local dynamical symmetry

In the upper panel of figure 11, we plot the scaled periods τ_{PO} of some POs as functions of the tetrahedral deofrmation parameter β_{td}. With increasing β_{td}, the scaled periods τ of the orbits DA and TB approach to each other. At $\beta_{td} = 0.502$, bifurcation of the diameter orbit DA takes place and a new three-dimensional orbit TD emerges. Subsequently, TD submerges into the three-dimensional rotational orbit TB at $\beta_{td} = 0.574$, shortly after its emergence. This is what we call a bridge orbit bifurcation [24]. Note that diametric DA and rotational TB are the orbits with minimum and maximum angular momenta. These greatly different orbits are connected by the bridge orbit TD within a small change of the shape parameter β_{td}. The same kind of the bridge bifurcations but in different pairs of POs take place almost simultaneously around $\beta_{td} = 0.5 \sim 0.6$, where we found a significant enhancement of the shell effect.

Here, we would like to remark that the bridge orbit bifurcation indicates a restoration of the dynamical symmetry around the trail of the bridge orbit connecting two mutually distant POs. Figure 12 illustrate how such a dynamical symmetry appears associated with the bridge orbit bifurcations. A local quasi-periodic family is formed around the first bifurcation where the DA bifurcates and the bridge TD emerges. Such a local family is also formed around the the second bifurcation where the orbit TD submerges into TB. Although the stationary points corresponding to the periodic orbits DA and TB are distinctly distant from each other, the two bifurcation deformations at the ends of the bridge are close together, which indicates a restoration of the dynamical symmetry in a large portion of the phase space including those three POs. In the tetrahedral RPL model, several bridge bifurcations take place simultaneously around $\beta_{td} = 0.5 \sim 0.6$, and the associated dynamical symmetry will also show up around all their replicas

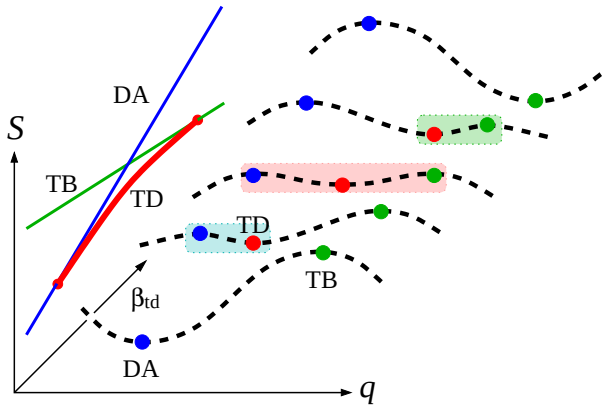

Figure 12. Illustration of the bridge-orbit bifurcation scenario. A family of quasi-periodic orbits (indicated by the shaded area) is generated in a large portion of the phase space connecting two POs, DA and TB, which are distant from each other in the phase space.

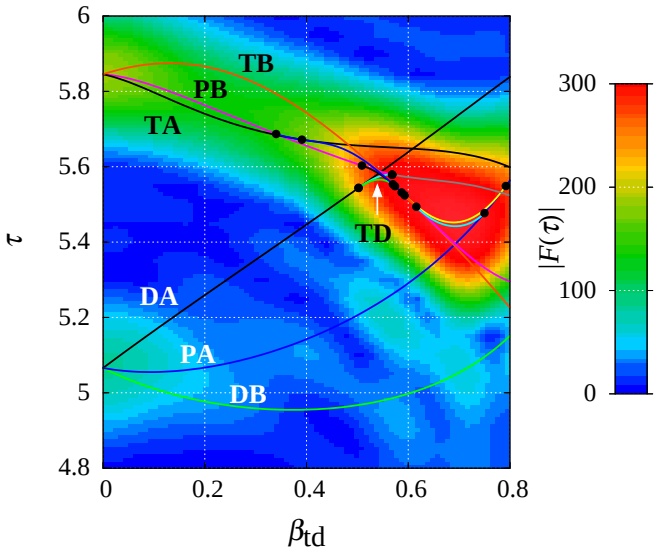

Figure 13. Quantum-classical correspondence in the Fourier transform of the level density. Color indicates the quantum Fourier amplitude $|F^{qm}(\tau;\beta_{td})|$, and the curves represent the scaled periods $\tau_{PO}(\beta_{td})$ of the classical POs.

related by the 24 symmetry transformations of the tetrahedral group T_d. Figure 13 shows the color map of the Fourier amplitude $|F^{qm}(\tau;\beta_{td})|$ as functions of τ and β_{td}. The scaled periods τ_{PO} of the classical POs are also drawn. The bifurcation points of those POs are indicated by the solid circles. This plot clearly shows us that the bridge orbit bifurcations around $\beta_{td} = 0.5 \sim 0.6$ are the origin of the anomalously strong shell effects found in Sec. 2.3. Considering together the agreement of the deformed magic numbers to those of the spherical HO model, one may expect a restoration of a large dynamical symmetry like SU(3).

4. Summary

The octupole deformed shell structures are investigated using the RPL potential model. Among the four types of pure octupole deformations, particularly strong shell effects are found for certain combinations of the power parameter α and the Y_{32}

deformation parameter β_{32}. The shell closures occur at particle numbers identical to the magic numbers in the spherical harmonic oscillator. The shell effect is found to be much more enhanced by taking the shape parametrization which smoothly connects the sphere and tetrahedron. Semiclassical analysis of the shell structure revealed its origin as the dynamical symmetry restoration associated with the bifurcations of bridge orbits between several pairs of short POs taking place at almost the same deformation $\beta_{\rm td}$. Fourier analysis of the level density clarified the correspondence between those bridge orbit bifurcations and enhancement of quantum shell effects.

In this peculiar type of the bifurcation scenario, two POs which are locating apart from each other in the phase space are connected by the bridge orbits, and families of quasi-periodic orbits are formed around them. In this sense, the bridge orbits play the roles of generators for the relevant hidden symmetries. If the six POs displayed in figure 8 are considered as the independent modes, the bridge orbit connecting two of those POs generates a symmetry between the corresponding two modes, and the number of the bridges may reflect the dimension of the symmetry. We have at least seven bridges between the above six POs, appearing almost simultaneously around $\beta_{\rm td} = 0.5 \sim 0.6$, and this number is close to 8, namely, the dimension of SU(3).

The shape parametrization (9) might be not realistic for nuclei due to the large curvatures around the four vertices of the tetrahedron. However, the shell effect is so large and we expect it to survive in a more realistic parametrization of the nuclear shapes, and probably, even after a reasonable spin-orbit coupling is switched on. Semiclassical studies on effects of the spin-orbit coupling to the tetrahedral shell structures are in progress.

Acknowledgement

The author thanks Prof. Jerzy Dudek and Prof. Kenichi Matsuyanagi for valuable discussions and comments.

References

[1] M. G. Mayer and J. H. D. Jensen, "Elementary Theory of Nuclear Shell Structure", Willey, New York (1955).

[2] A. Bohr and B. R. Mottelson, "Nuclear Structure", Vol. I, Benjamin, New York (1969).

[3] P. Ring and P. Schuck, "The Nuclear Many-Body Problem", Springer-Verlag, New York (1980).

[4] C. Bahri, P. J. Draayer and S. A. Moszkowski, Phys. Rev. Lett. **68**, 2133 (1992)

[5] W. Nazarewicz and J. Dobaczewski, Phys. Rev. Lett. **68**, 154 (1992).

[6] M. C. Gutzwiller, J. Math. Phys. **8**, 1979 (1967); **12**, 343 (1971).

[7] R. Balian and C. Bloch, Ann. Phys. (NY) **69**, 76 (1972).

[8] V. M. Strutinsky, A. G. Magner, S. R. Ofengenden and T. Døssing, Z. Phys. A **283**, 269 (1977).

[9] M. Brack and R. K. Bhaduri, "Semiclassical Physics", Westview Press, Boulder (2003).

[10] K. Arita, Physica Scripta **91**, 063002 (2016).

[11] P. A. Butler and W. Nazarewicz, Rev. Mod. Phys. **68**, 349 (1996).

[12] J. Dudek *et al*, Phys. Rev. Lett. **97**, 072501 (2006).

[13] J. Dudek *et al*, Int. J. Mod. Phys. E **16**, 516 (2007).

[14] M. Yamagami, K. Matsuyanagi and M. Matsuo, Nucl. Phys. A **693**, 579 (2001).

[15] S. Tagami, Y. R. Shimizu and J. Dudek, Phys. Rev. C **87**, 054306 (2013).

[16] I. Hamamoto, B. Mottelson, H. Xie and X. Z. Zhang, Z. Phys. D **21**, 163 (1991)

[17] S. M. Reimann *et al*, Phys. Rev. B **56**, 12147 (1997).

[18] K. Arita, Phys. Rev. C **86**, 034317 (2012).

[19] K. Arita and Y. Mukumoto, Phys. Rev. C **89**,054308 (2014).

[20] V. M. Strutinsky, Nucleonika (Poland) **20**, 679 (1975).

[21] V. M. Strutinsky, A. G. Magner, Sov. J. Par. Nucl. **7**, 138 (1976).

[22] M. Sieber, J. Phys. A **29**, 4715 (1996).
H. Schomerus and M. Sieber, J. Phys. A **30**, 4537 (1997).
M. Sieber and H. Schomerus, J. Phys. A **31**, 165 (1998).

[23] A. G. Magner, S. N. Fedotkin, K. Arita, T. Misu, K. Matsuyanagi, T. Schachner and M. Brack, Prog. Theor. Phys. **102**, 551 (1999).
A. G. Magner, K. Arita, S. N. Fedotkin and K. Matsuyanagi, Prog. Theor. Phys. **108**, 853 (2002).

[24] K. Arita and M. Brack, J. Phys. A **41**, 385207 (2008).